Check for updates

OPEN

Geophysical early warning of salt precipitation during geological carbon sequestration

Ismael Himar Falcon-Suarez[1✉], Kurt Livo[2], Ben Callow[1,3], Hector Marin-Moreno[1,4], Manika Prasad[2] & Angus Ian Best[1]

Sequestration of industrial carbon dioxide (CO_2) in deep geological saline aquifers is needed to mitigate global greenhouse gas emissions; monitoring the mechanical integrity of reservoir formations is essential for effective and safe operations. Clogging of fluid transport pathways in rocks from CO_2-induced salt precipitation reduces injectivity and potentially compromises the reservoir storage integrity through pore fluid pressure build-up. Here, we show that early warning of salt precipitation can be achieved through geophysical remote sensing. From elastic P- and S-wave velocity and electrical resistivity monitoring during controlled laboratory CO_2 injection experiments into brine-saturated quartz-sandstone of high porosity (29%) and permeability (1660 mD), and X-ray CT imaging of pore-scale salt precipitation, we were able to observe, for the first time, how CO_2-induced salt precipitation leads to detectable geophysical signatures. We inferred salt-induced rock changes from (i) strain changes, (ii) a permanent ~1.5% decrease in wave velocities, linking the geophysical signatures to salt volume fraction through geophysical models, and (iii) increases of porosity (by ~6%) and permeability (~7%). Despite over 10% salt saturation, no clogging effects were observed, which suggests salt precipitation could extend to large sub-surface regions without loss of CO_2 injectivity into high porosity and permeability saline sandstone aquifers.

Deep siliciclastic saline aquifers are among the preferred options for geological CO_2 sequestration (GCS), because of their low reactivity to CO_2 and high storage capacities[1]. The storage efficiency is determined by the porosity (reservoir capacity), while the effectivity of the injection is controlled by the permeability (connectivity of the effective pore volume). Any changes in the storage capacity and/or injection efficiency during GCS activities may compromise the integrity of the reservoir[2,3], and hence needs further study for long-term and safe sequestration of CO_2.

The CO_2 injected in a reservoir advances as a plume by displacing a fraction of the resident brine[4,5]. The injected CO_2 partially dissolves in the parent brine while inducing evaporation of water. These two mechanisms, together with capillary pressure gradients towards the injection source, molecular diffusion of saline ions within the brine, CO_2 gravity (buoyancy) and self-enhancing salt crystallization phenomena, can trigger complex salt precipitation patterns in porous media[6]. CO_2-induced salt precipitation can lead to a significant decrease of up to 15% in porosity, and up to 85% in permeability[7]. Eventually, this phenomenon can dramatically impact the injection efficiency, as observed off-shore in the Tubåen Formation at the Snøhvit Field[8].

Several studies have addressed the mechanisms and location of salt precipitates in saline aquifers during CO_2 storage, and the negative consequences for the injectivity[9–14]. Numerical simulations predict significant salt-induced pressure build-up around the CO_2 injection well, the preferential salt precipitation area[15–17], even for high permeability rocks and low injection rates[18,19]. Experimental studies have confirmed CO_2—induced salt precipitation in porous media from lab-on-chip experiments[6,20] and core scale flow-through tests[21–23]. Experimental observations show that the precipitation process starts after a transition period post—CO_2 injection, forming early pore scale crystals in the brine, followed by late polycrystalline aggregates at the CO_2—brine interface[7]. The velocity and extent of the process depend on CO_2 injection flow rate[18], brine mobility[24], pore network geometry[19],

[1]National Oceanography Centre, University of Southampton, Waterfront Campus, European Way, Southampton SO14 3ZH, UK. [2]Colorado School of Mines, Golden, CO 80401, USA. [3]University of Southampton, National Oceanography Centre Southampton, Southampton SO14 3ZH, UK. [4]Norwegian Geotechnical Institute, Ullevål Stadion, PB 3930, 08906 Oslo, Norway. ✉email: isfalc@noc.ac.uk
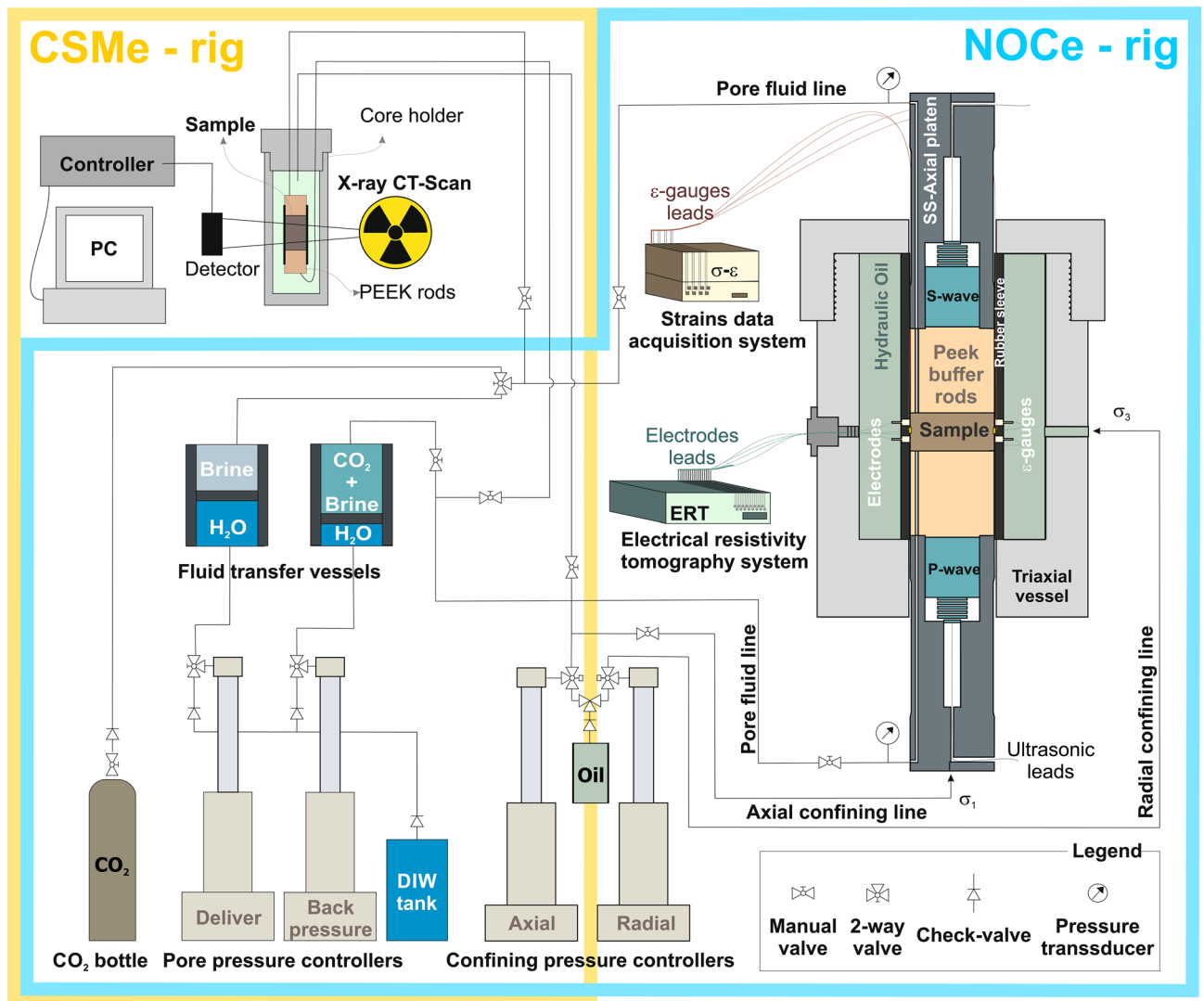
1

Figure 1. CSMe and NOCe experimental rigs.

and the physical properties of both fluids defined by the temperature, pressure and composition[25,26], particularly brine salinity[7].

Simple engineering mitigation strategies can be applied in the reservoir to prevent the salt precipitation during CO_2 injection activities in the field. For instance, fresh water-washing—a technique originally used in gas-producing wells to avoid salt clogging[16] that has been proposed for GCS prior to CO_2 injection[7,17,27]. Early detection of salt precipitation is crucial for timely mitigation strategies and ultimately for preserving reservoir integrity. However, this requirement contrasts with the lack of experimental and modelling studies aimed at the identification of CO_2—induced salt precipitation from field-scale monitoring datasets, especially geophysical remote sensing.

We conduct CO_2 flow-through tests, using a high porosity–permeability non-reactive sandstone to isolate the CO_2-induced salt precipitation phenomenon. Here we integrate elastic and electrical resistivity measurements, X-ray micro-CT imaging, and rock physics modelling, to assess the potential of combined seismic and electromagnetic surveys for early detection of CO_2—induced salt precipitation.

Core flood experiments. This study involves two CO_2 injection experiments (denoted as CSMe and NOCe) on a high porosity ($\sim 29\%$), high permeability (~ 1660 mD) synthetic quartz-rich sandstone, saturated with high salinity ($X_{NaCl} = 25\%$ wt. NaCl) synthetic brine. The experiments were conducted using two experimental setups for high pressure multi-phase flow-through tests (CSMe and NOCe rigs, Fig. 1), under constant hydrostatic confining pressure ($P_c = \sigma_1 = \sigma_2 = \sigma_3 = 25$ MPa), pore pressure ($P_p = 5.5$ MPa), and room temperature (~ 20 °C).

CSMe aimed at analysing the distribution of CO_2, brine, and CO_2-induced precipitation of salt crystals in the rock using micro-X-ray computed tomography (XCT) scans. In the first step, 17 pore volumes (PV) of brine were injected through the rock at a flow rate of ~ 0.2 cm^3 min^{-1}, followed by a XCT (lasting ~ 24 h). Next, CO_2 gas

($CO_{2(g)}$) was injected into the sample at ~ 0.2 cm^3 min^{-1} continuously for 24 h (~ 200 PV), followed by a second XCT scan (~ 24 h). From the XCT, we developed a four-phase segmentation analysis to obtain the CO_2, brine, quartz grain and salt volumetric fractions. Then, the sample was dried, cut and prepared into thin sections to compare with the original sample to assess the total salt content in the porous medium. Finally, the sample was subjected to X-ray diffraction (XRD) and scanning electron microscopy with energy dispersive spectroscopy (SEM–EDS) analysis to assess the precipitation of secondary minerals resulting from the CSMe test (see Supplementary Information). For the thin section analysis, we developed a three-phase (pore space, quartz grain and salt) segmentation analysis.

In the NOCe, we measured geophysical (ultrasonic compressional and shear, P and S, wave velocities and electrical resistivity) and hydro-mechanical (axial strains) properties, under three flooding conditions: (i) initial 25% NaCl brine flow-through the brine saturated sample (~ 10 PV); (ii) $CO_{2(g)}$ injection flow displacing the brine from the saturated sample (drainage episode; ~ 75 PV); and (iii) 25% NaCl brine flow through the partially CO_2 saturated sample (imbibition episode; ~ 30 PV). During the test, we alternated between two flow (Q) regimes: active measuring periods when Q was above 0, and interludes (Q = 0) without data collection. The test was repeated twice, named hereafter as NOCe Test-1 and Test-2, respectively.

Results and discussion

Salt saturation estimate (CSMe). XCT image analysis (Fig. 2) shows that CO_2 and brine occupied 42% and 50% of the total pore volume, respectively, after CO_2 injection (i.e., second scan), yielding a salt saturation (S_{NaCl}) of ~ 8% (Table 1). During the scanning the vessel was sealed, limiting the brine salinity to the dissolved ions within the pore water. Considering that the XCT scan lasted ~ 24 h, S_{NaCl} likely increased during scanning and therefore 8% represents a lower bound of S_{NaCl} in the CO_2-brine-rock system after two days of CO_2 exposure (i.e., one day of CO_2 injection and one for the scan).

Theoretically, using mass balance considerations, in our closed system, one single halite crystal of density $\rho_{NaCl} = 2100$ kg m^{-3} formed from the brine (S_{brine}, with density $\rho_{brine} = 1190$ kg m^{-3} and salinity $X_{NaCl} = 25\%$ wt) occupying the available pore space post-test (i.e., 1 – S_{CO2}) would fill 8.2% of the total pore volume (i.e., $S_{NaCl(theoretic)} = (1—S_{CO2}) \cdot X_{NaCl} \cdot \rho_{brine}/\rho_{NaCl}$). However, thin section analysis (Fig. 3) reveals the subsequent drying process led to a final $S_{NaCl(observed)}$ ~ 19% (± 2% derived from 2D-thin section to 3D transformation[28]). This analysis indicates that the salt precipitates around the rock grains mainly as an agglomerate of halite microcrystals, as previously observed[6]. This finding is corroborated by SEM–EDS analysis (Fig. 4) and XRD post-testing, which also shows NaCl crystals sometimes coexisting with nahcolite (NaHCO$_3$) as subsidiary (further information in Supplementary Information). For practical reasons, we adopt the physical properties of the major component observed (i.e., halite) for the whole salt fraction and estimate a salt-aggregate micro-porosity of ~ 56.7% ± 2%, resulting from the ratio between theoretical and thin-section estimated S_{NaCl} post-test ($\phi_{NaCl,micro} = 1 – S_{NaCl(theoretic)}/S_{NaCl(observed)}$). This micro-porosity fraction is below the image resolution for both the XCT and thin section processing. Accounting for this micro-porosity, the S_{NaCl} determined from XCT scan drops to 3.5%, indicating the salt precipitation was still in an early stage after two days exposed to CO_2.

Geophysical data analysis (NOCe). The NOCe $CO_{2(g)}$ injection test lasted approximately five days (~ 115 h) and it was repeated twice, with an effective flow-through time of ~ 40 h that led to ~ 110 pore volumes (PV) throughput each (Fig. 5). Both tests show similar trends for all the measured properties except for the strains. Around 2% hysteresis effect of P- and S-wave velocities (V_P and V_S) suggests a change in the physical properties of the sample during the experiment. On the other hand, the transport properties of the sample remained undiminished (under the experimental conditions), as indicated by an almost constant pore pressure gradient (ΔP_p) throughout the NOCe for each pore fluid (i.e., brine flow in E1$_{brine}$ and E5; CO_2 from E1$_{CO2}$ to E4) within the range of flow rates 0–2 cm^3 min^{-1}.

The CO_2 arrival (episode E1$_{CO2}$ after 9 PV of brine flow; Fig. 5), led to a resistivity increase of ~ 50%. Electrical resistivity tomography (ERT) images (Fig. 6) show preferential pathways localized peripherally by the inlet–outlet ports on the axial platens (diagonally opposite one other); the invariant differential pore pressure for changing flow-rates suggests the preferential pathways remained active through the test[29]. This annular fluid distribution provides very little variations on V_P and V_S. Hence, the brine was first mainly drained from the edges of the sample whereas the CO_2 is progressively saturating the resident brine towards the centre. Water evaporation rate into the CO_2 stream is very low during this step[23]. This behaviour might indicate early salt precipitation acting as a lateral permeability barrier for CO_2 advance towards the central part of the sample[18].

After the initial gas-pushing water piston fluid substitution effect [30], each interlude leads to a redistribution of the two-phase fluids due to capillary effects that enhances salt precipitation[7,26]. During the interlude E1-E2, in the absence of effective pressure variations, the axial strain (ε_a) increased (more significantly during the first test; Fig. 5). Since our quartz-rich sandstone is barely reactive to CO_2, we interpret sample dilation as being caused by local salt-induced volumetric increase effects, previously observed in CO_2-brine tests in sandstones under hydrostatic confining conditions[31] and in air-brine systems under uniaxial loading[32]. In this regard, it has been recently demonstrated[33] that salt crystals may exert pressures against pore walls up to ten times higher than the confining pressure used here (up to 150 MPa at the 50 μm observation microscale). Sample dilation continued during episode E2 accompanied by a weak decrease in both V_P and V_S by ~ 2%, and a resistivity increase by ~ 25%, in agreement with previously reported data[5,31,34–37]. Overall, E1 and E2 have similar pore fluid distributions (Fig. 6), and small geophysical variations, which can be explained by minor mechanical-chemical changes in the outer part of the sample.

The most significant changes in the elastic properties of the rock sample occur after the second interlude (from E2 to E3; Fig. 5), with V_P and V_S increasing by ~ 3% and V_S ~ 0.5%, respectively, in both tests. These changes
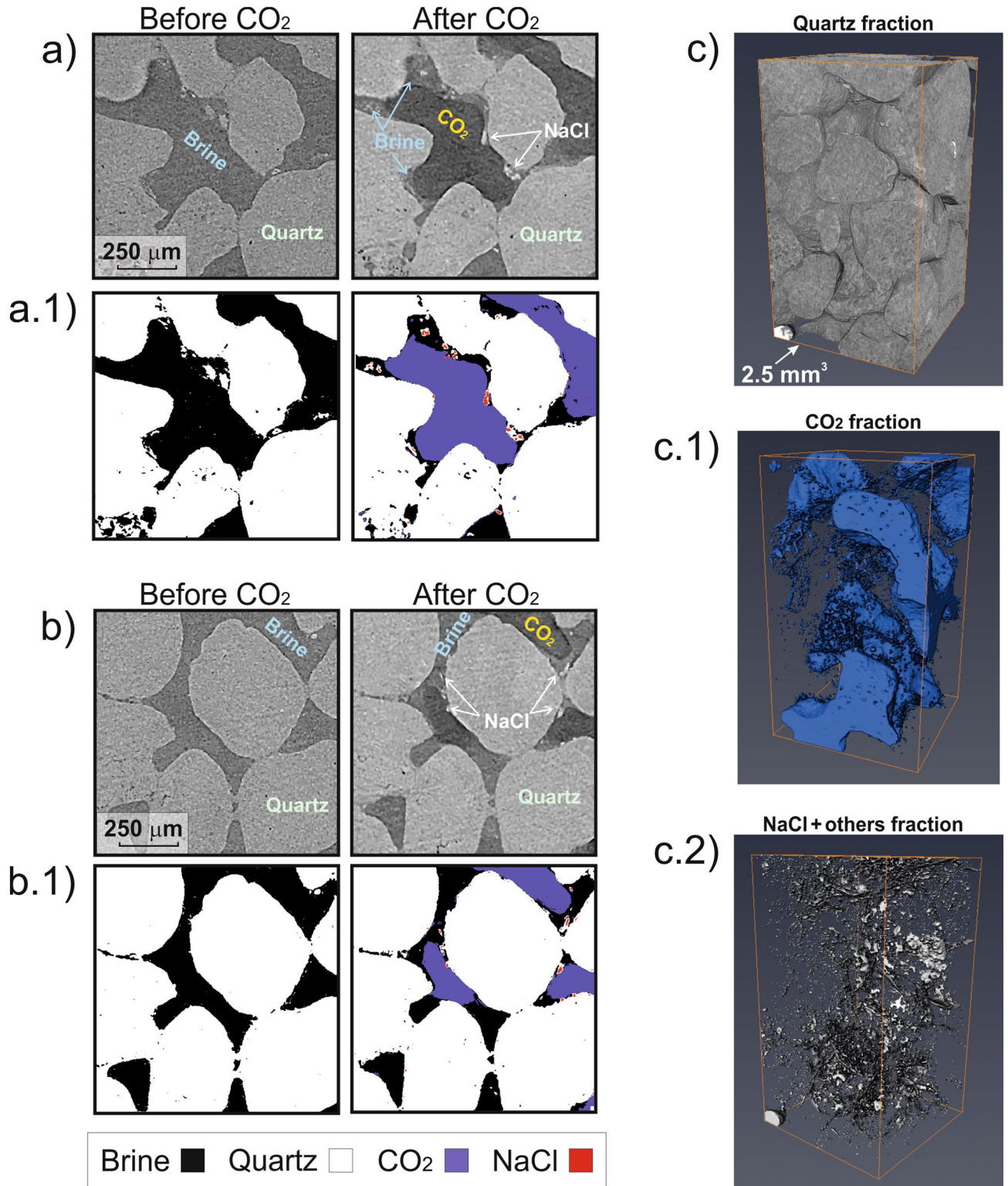
Figure 2. Salt precipitation evidence from the sandstone used in the CSMe. Examples of XCT scans before and after CO_2 injection in 2D (**a, b**), and 3D (**a** 2.5 mm³ volume portion) post-CO_2 injection (**c** 1–3), including segmentation (**a.1, b.1, c.1–c.2**).

contrast with the positive deformation of the sample (i.e., inflation) and the theoretical lowering of V_P for an increasing CO_2 content[5,36]. However, our results agree with the scarce data reported about changes of elastic wave properties associated with salt precipitation in high porosity sandstone[8,38]. During E3 and E4, resistivity, strains,

CT-Run (CSMe)	Volume fractions (%)[a]				Saturation		
	CO$_2$	Brine	Quartz	NaCl[b]	S$_{NaCl}$	S$_{CO2}$	S$_{brine}$
Before CO$_2$	0	29.7	69.6	0.7			
After CO$_2$	12.7	15.1	69.0	3.2	0.08	0.42	0.50
Thin sections	Area fractions (%)						
	Pores	Grains	NaCl[b]	S$_{NaCl}$			
Original sample	27.5 ± 0.5	71.4 ± 0.5	2.1 ± 0.2	0.0			
Fully dried after CSMe	22.5 ± 1.0	67.5 ± 1.0	10 ± 0.2	~ 0.19			

Table 1. XCT scan and thin section processed results. [a]General volume fraction error of 1% and saturation uncertainty of ± 0.01. [b]NaCl phase contains NaCl plus others isotropic minerals.
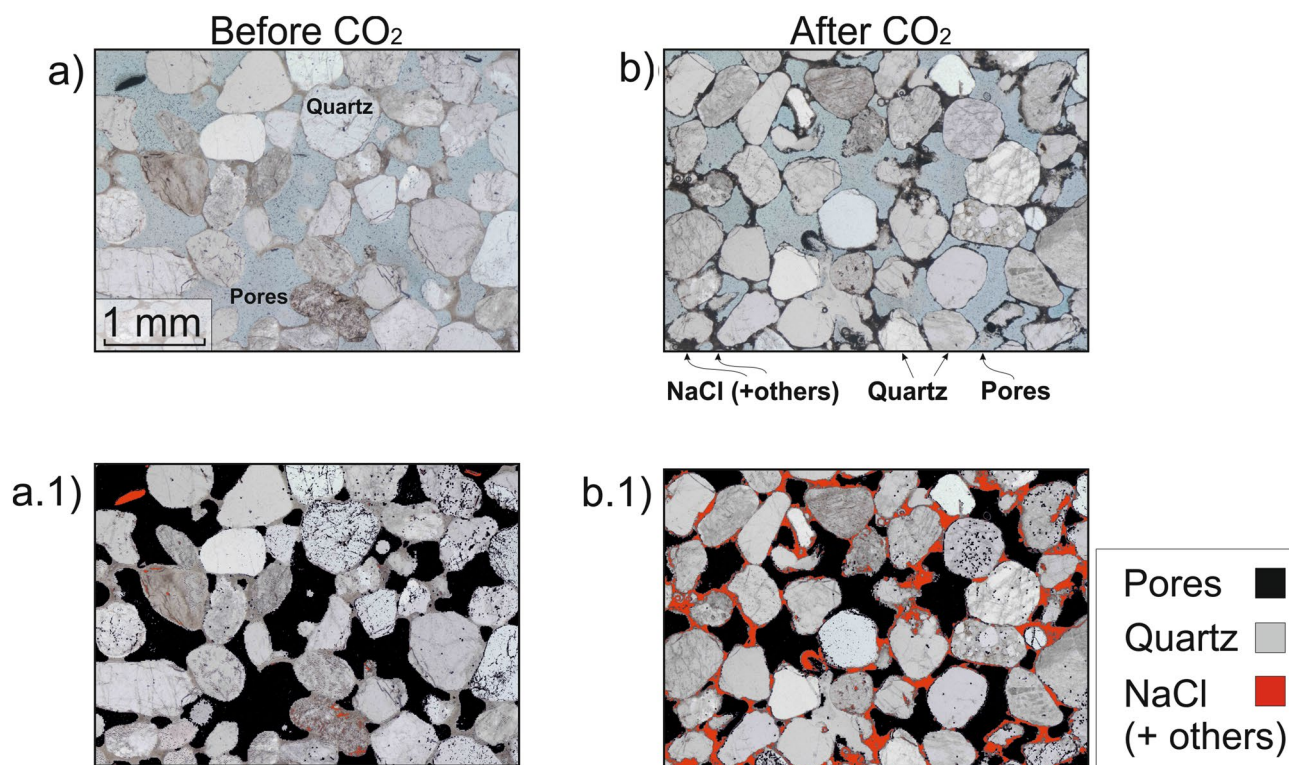
Figure 3. Salt precipitation evidence from thin sections of **(a)** the original sandstone used in the CSMe and **(b)** after full drying post-testing, including segmentation **(a.1, b.1)**.

and V$_S$ progressively increase while V$_P$ decreases with CO$_2$ injection. Despite a few sharp variations seen for all the parameters during the interlude E3–E4, E3 and E4 show similar trends that agree with those previously observed during CO$_2$-brine drainage tests in sandstone[31,34,36,37,39]. During the last episode (E5, forced imbibition), the original brine flows through the sample, partially saturated in CO$_2$. All the measured parameters recover to their original values except axial strains in barely five PV (Figs. 5, 6), a rapid recovery previously observed in CO$_2$-brine-quartz systems under imbibition[31,35]. Resistivity totally recovered its original values. V$_P$ and V$_S$ carry ~ 1% of negative hysteresis at the end of the first test, and up to 1.5% after the second, with a minimum decrease from the end of Test-1 to start of Test-2. After the NOCe Test-2, the sample showed an increase of the original porosity, by ~ 6%, and permeability, by 7%.

Saturation uncertainties. In a natural reservoir, a constant brine salinity scenario should be expected provided that salt clogging does not occur; in our test, the brine salinity progressively decreases as salt saturation increases. Since we calculate pore fluid saturations from the measured electrical resistivity and Archie's laws[31,35], we must first consider any changes in brine salinity caused by the CO$_2$ drying process. The observed changes in bulk resistivity are mainly related to (i) a fluid substitution effect (i.e., high resistive CO$_2$ displacing the original brine in the porous medium), and (ii) a progressive decrease of the original brine salinity with CO$_2$ (i.e., ions-depleted residual brine due to salt precipitation). Each of these two factors reduces resistivity and affects the transformation of electrical resistivity into saturation differently.
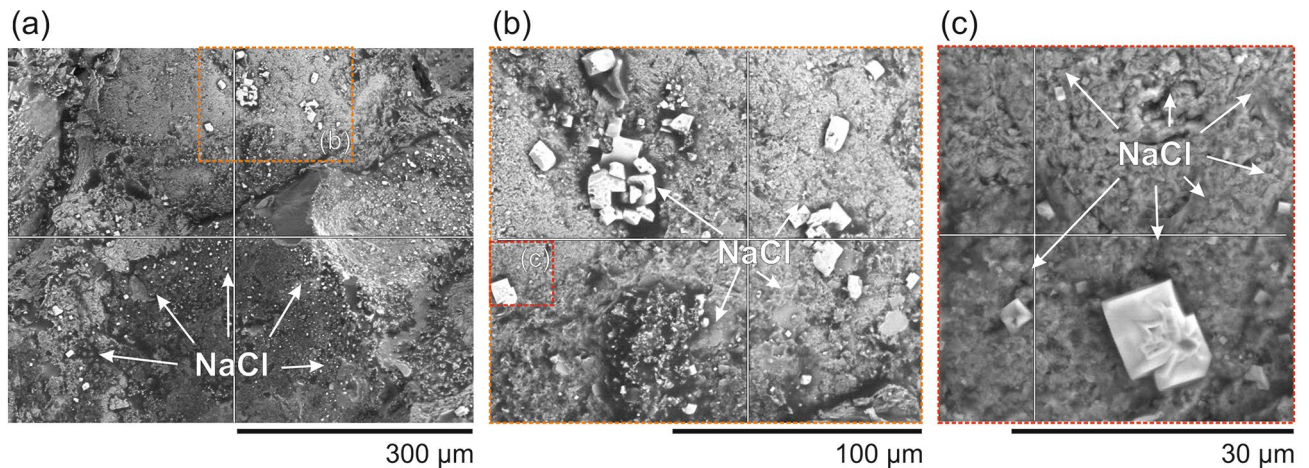
Figure 4. Scanning electron microscope (SEM) images showing salt crystals (NaCl) coating the original sample grains, in three zoom-in scales (from **a** to **c**), after full drying post-testing, corroborated by Energy Dispersive Spectroscopy (EDS) analysis (Supplementary Information).

Pore fluids saturation in a CO_2-brine system can be calculated from electrical resistivity[31,34,36,39], combining the first, $\Phi^{-m} = \frac{R_{b,0}}{R_w}$, and second, $S_w^n = \frac{R_w}{R_{b,i}} \Phi^{-m}$, Archie's laws for fully and partially saturated porous media[40], respectively. In these expressions, R_b is the bulk resistivity of the sample with subscripts 0 and i indicating full and partial saturation, R_w is the resistivity of the pore fluid, ϕ the porosity, S_w the brine saturation, and m and n are the cementation and saturation exponents, empirically derived for each particular rock.

The dissolved CO_2 (less than 5% vol. at the experimental conditions[41,42]), is invisible to our resistivity and ultrasonic detection tools[35], and therefore neglected in the saturation calculations based on Archie's expressions above. This simple transformation is valid for invariable porous framework systems, i.e., in the absence of dissolution/precipitation phenomena. However, the XCT scanning showed a minimum S_{NaCl} (aggregate microcrystalline) of 8% for our experiments. CO_2-induced salt growth progressively changes the bulk electrical properties of the rock, by changing both the porosity and brine resistivity. Therefore, to calculate S_w, the combination of the first and second Archie's laws has to be modified to account for each state of the rock with respect to the original values (subscripts i and 0, respectively), as follows:

$$S_w^n = \frac{R_{b,0}}{R_{b,i}} \frac{R_{w,i}}{R_{w,0}} \tag{1}$$

In Eq. (1), we consider constant cementation (m) and saturation (n) exponents, because the salt aggregates observed in our CSMe test are suspended at the CO_2-brine interface (Fig. 2). However, the cementation exponent is likely to increase in more advanced drying stages. Note that the change in water resistivity between stages is explicitly considered in Eq. (1), but the change in porosity due to salt precipitation is not. The micro-metre salt crystals are surrounded by highly conductive water films feeding the crystallization process[6].

At laboratory conditions (20 °C), if we consider a closed system where all the original brine contributed its ions to halite formation, the R_w would have increased according to the expression[43] $R_w = \left(4 \times 10^5 / TS\right)^{0.88}$, with S being the brine salinity (in ppm) and T the temperature (in Fahrenheit). However, some backflow of brine towards the injection point[17], particularly during interludes, might have partially contributed to salinity recovery. We consider the transition between a backflow completely renewing the resident brine (i.e., constant salinity), to no backflow leading to a progressively NaCl-depleted brine (Fig. 7). In our test, the degree of brine saturation estimated from bulk resistivity data should lie between both cases.

Combining elastic and electrical properties. Salt can form either away from the mineral grains (non-cementing salt), or at grain contacts bridging mineral grains (cementing salt). Image analysis suggests a transition from non-cementing salt at early stages of salt formation (XCT images; Fig. 2) to cementing salt after fully drying (thin sections; Fig. 3). Early detection of this transition in the field using geophysical monitoring techniques is essential to initiate mitigation strategies in a timely manner, before both injectivity and ultimately the mechanical integrity of the reservoir are compromised (as suggested by the mechanical hysteresis observed in our data).

The bulk elastic properties of rocks are sensitive to the rock frame and pore fluid elastic properties[44], and to the distribution of fluids in the porous medium for multiple fluids (e.g., uniform/patchy[45]). Hence, to infer such a transition in the salt distribution from our geophysical data, we can use the so called uncemented and cemented sand models[46,47], and introduce them into Biot-Stoll poroelastic formulation[48–50] to calculate frequency-dependent P and S wave velocity and attenuation. This approach has been applied previously to understand and assess quantitatively the impact of marine methane hydrate on these properties[51,52]. Due to the similarities in the distribution of hydrate and salt in the pores, we adopt these models using the physical properties (bulk and shear moduli, and density) of halite.
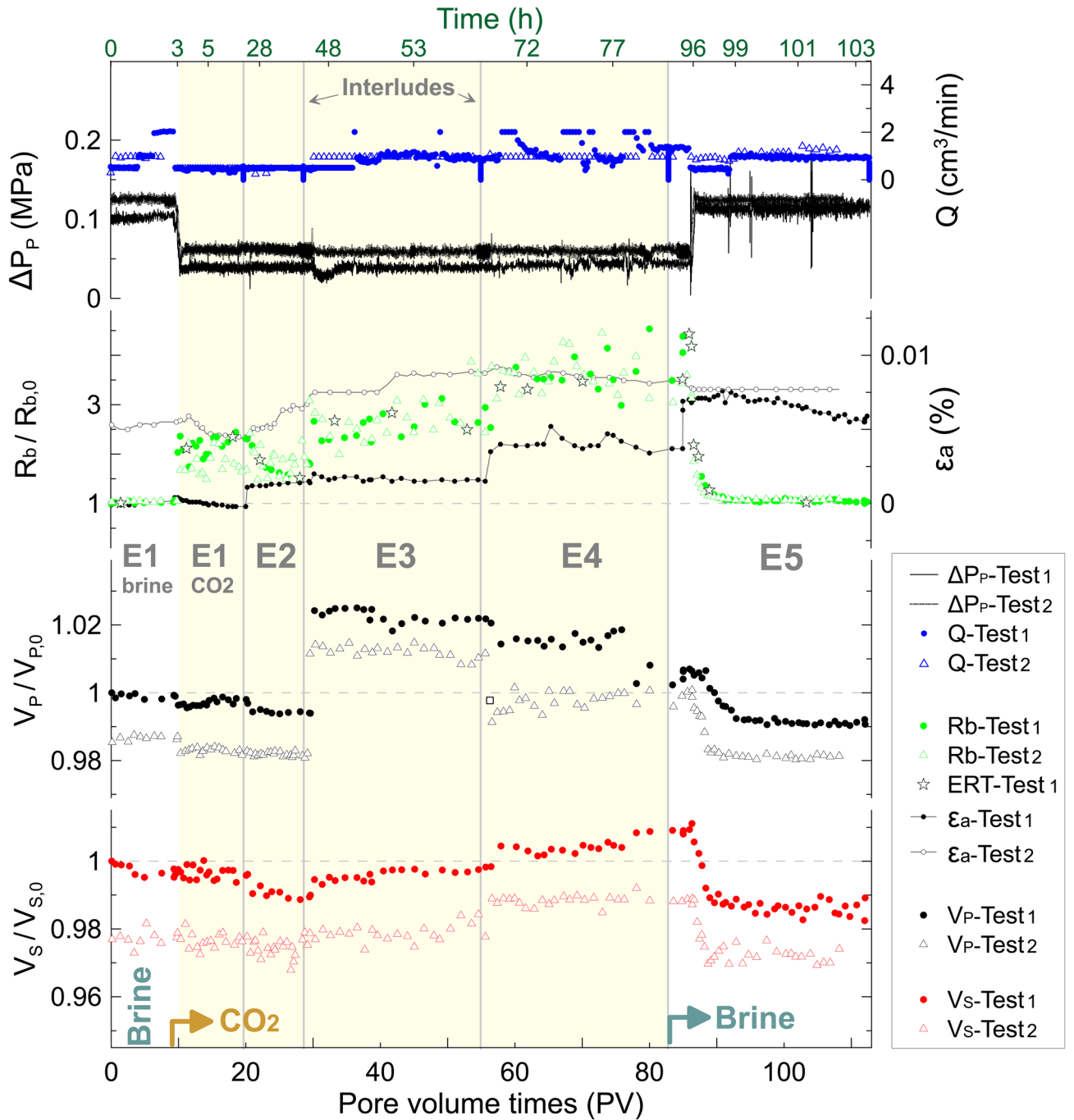
Figure 5. Results of two consecutive brine-CO_2 flow-through tests (Test-1, black solid line and solid dots; Test-2, grey solid line and open triangles) in synthetic sandstone during the NOCe. Up- and downstream differential pore pressure (ΔP_p) and total outlet flow (Q), P- and S-wave velocities (V_P, V_S), bulk electrical resistivity (R_b), and axial strains (ε_a in %) are plotted versus pore volume (PV) and experimental time for three flooding episodes (E): brine flow (E1$_{brine}$, below 9 PV), CO_2 replacing brine (E1$_{CO2}$ to E4; drainage), and brine replacing CO_2 (E5; imbibition). Geophysical properties and strains are presented normalized with respect to initial values of Test-1. Solid vertical lines indicate interludes between episodes (i.e., Q = 0).

Using these model predictions, we can explain the observed evolution of the CO_2-brine-salt-sandstone system from changes in the compressional and shear wave velocities with brine saturation, with both the NOCe Test-1 and Test-2 showing very similar results (Fig. 8). We assume that non-cementing salt only modifies the bulk modulus of the fluid. In contrast, cementing salt modifies both the shear and bulk moduli of the dry granular frame. Hence, V_S can be significantly affected by cementing salt but not by non-cementing salt (only minor changes can occur due to changes in bulk density of the rock).
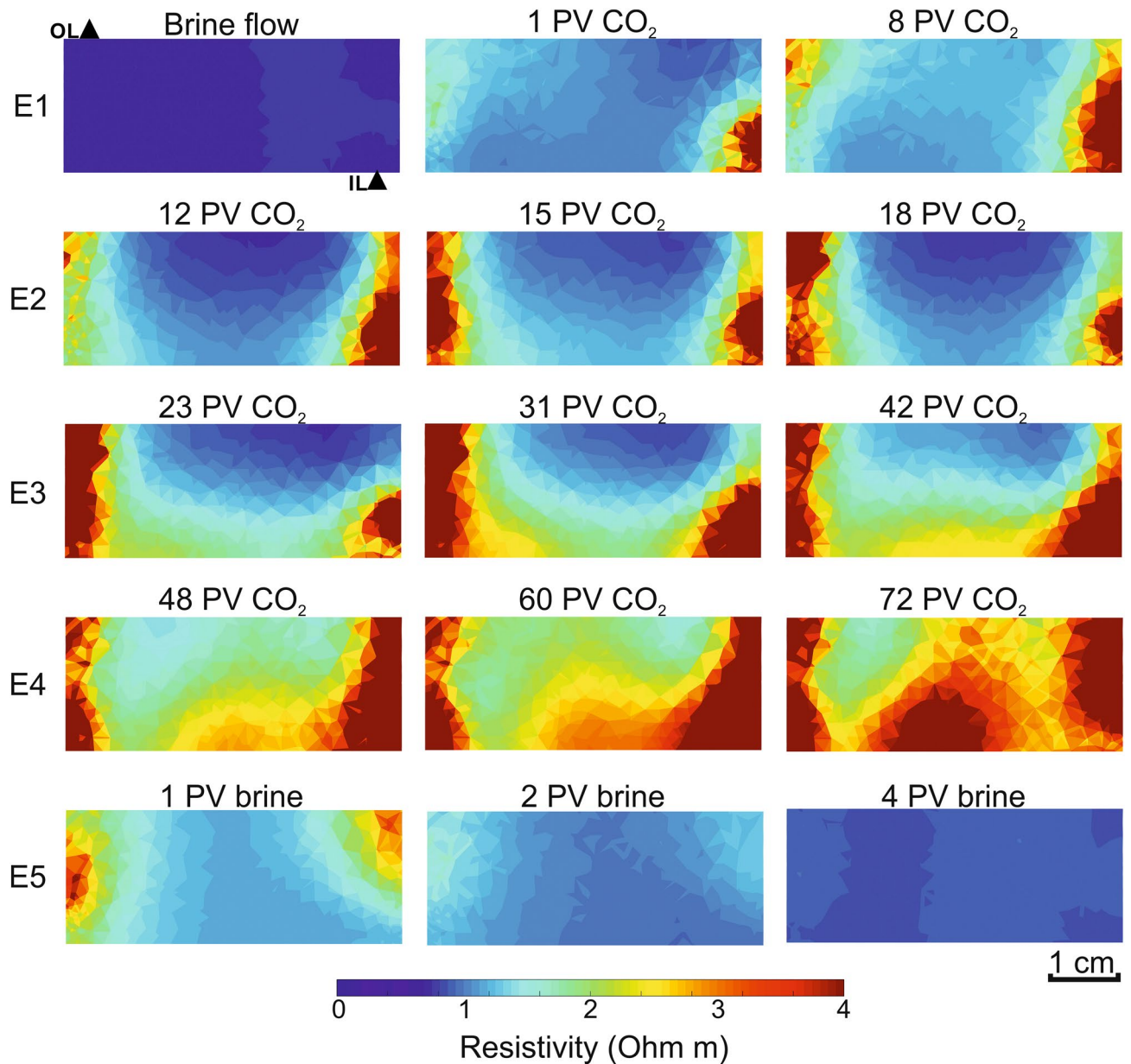
Figure 6. 2D electrical resistivity tomography acquired during the NOCe Test-1 (star points in Fig. 5). The images are vertical planes crossing the centre of the sample, containing the inlet (IL) and outlet (OL) pore fluid ports as marked by solid triangles.

For P-waves, the change in V_P from $E1_{brine}$ (brine flow) to $E1_{CO2}$ (CO_2 flow) can be explained by the presence of up to ~ 4% of solid non-cementing micro-crystalline NaCl into the pore space during Test-1 (~ 2% for Test-2), partially reabsorbed during the interlude E1-E2 (Fig. 8a). The most significant change in V_P occurs from E2 to E3. During this interlude, the drying through evaporation is likely to be enhanced by capillary and diffusive mechanisms, leading to a higher crystallization rate[7,26]. The model indicates a sharp S_{NaCl} increase from E2 (S_{NaCl} ~ 1%) to E3 (S_{NaCl} ~ 13% in Test-1 and ~ 14% in Test-2). The brine remaining in the pore space is then NaCl-depleted and salt crystallization stabilizes, leading to a (CO_2—brine) fluid substitution stage with some salt reabsorption phenomena at the end of the episode E4.

For S-waves, V_S reflects an early rock weakening effect during the transition from brine to CO_2 injection (V_S drops from $E1_{brine}$ to $E1_{CO2}$), likely associated with poorly attached silica cement or grains, removed during early stages of the CO_2 flooding due to sudden changes in the bulk properties (i.e., early salt nucleation) of the pore fluid (Fig. 8b). This early weakening effect is observed in both NOCe tests, but more significantly in Test-1. To isolate the CO_2-induced salt precipitation effect after this early weakening, we project the modelling results to fit the data after $E1_{CO2}$ (grey bands and grey lines in Fig. 8b) by considering the final V_S value of each test as $V_{S,0}$. From $E1_{CO2}$ to E3, the V_S data scatter (within the ultrasonic measurements error band) over the whole range of results for the non-cementing salt modelling (i.e., S_{NaCl} from 0 to 14%). The clear increase in V_S from E3 to E4
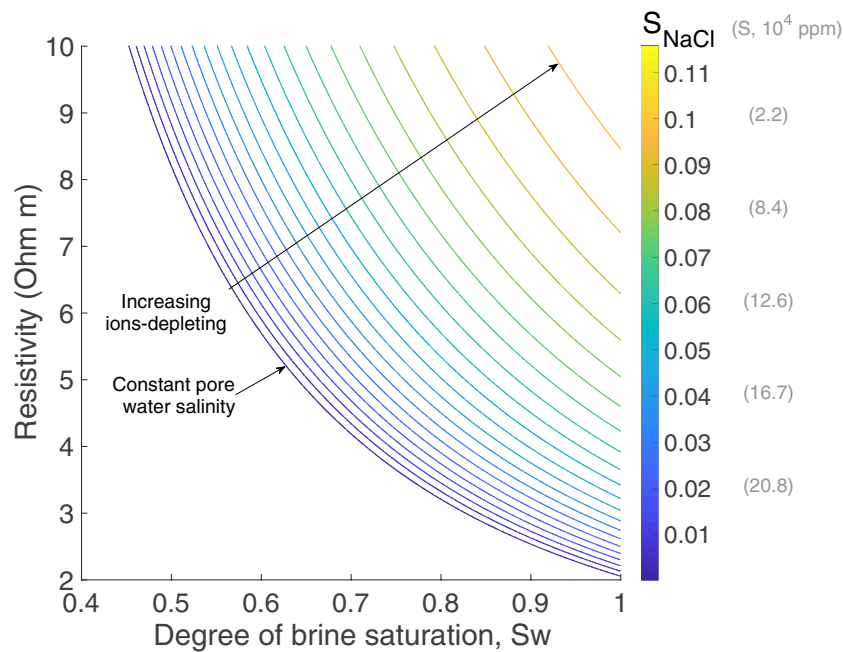
Figure 7. Bulk resistivity versus degree of brine saturation considering an initial brine salinity (S) of 25×10^4 ppm, a constant temperature of ~ 20 °C, and the ions-depleting effect associated with the precipitation of salt (S_{NaCl}, salt saturation) in a closed system.

can be explained by considering a transition (red arrows in Fig. 8) from only non-cementing salt in E3, to non-cementing salt with a small fraction (0.1%) of cementing salt in E4 (red curve in Fig. 8); grey solid curve for the projection in Fig. 8b). Finally, brine is injected into the sample, and rapidly replaces (and dissolves) the salt-rich CO_2-brine mixture in the pore space.

For a precise quantification of the evolution of the three pore phases, we would need to account for the progressive ions depletion of the original brine, which could be significant, as shown in Fig. 7; this would require monitoring of pore water conductivity during the CO_2 flooding, which is missing in this experiment. Instead, we have added one single horizontal error bar to reflect the uncertainty associated with the increasing pore water resistivity for each episode (E1–E5).

The transition from non-cementing to cementing salt (E4) occurs after a substantial S_{NaCl} increase from E2 to E3 of (from ~ 2 to ~ 12% in Test-1 and up to ~ 14% in Test-2) well-defined by ~ 3% increase in V_P (Fig. 8a). This rapid S_{NaCl} increase occurs in the absence of CO_2 flow (interlude E2–E3). By contrast, during flowing episodes, changes in rock properties are better explained by fluid substitution mechanisms as data points within each episode evolve towards higher CO_2 saturations.

Insights of salt distribution in geological reservoirs. From the constant response of our pore pressure sensors for different flow rate conditions all through the NOCe tests, we conclude that any clogging effects due to salt induced porosity reduction were insignificant. The distribution of gas-induced salt precipitation in a porous medium can be described through the Peclet ($P_e = LV/D$), and Damköhler ($Da = Lk_r / V$ for Pe > 1[53]) numbers (reference length, L; effective flow velocity, V; diffusion coefficient of salt in water, D; kinetic rate constant, k_r). Pe determines the importance of advective (Pe > 1) and diffusive (Pe < 1) transport[54], while Da describes to which extent the dissolution/precipitation processes are dominated by fluid velocity or mineral reactivity[53]. For Pe > > 1, salt precipitation would occur close to the injection zone, whereas Pe < < 1 would lead to a homogeneous distribution[23]; the crystallization process is controlled by diffusion when Da > > 1[55]. In our closed system, the calculation of Da is not straightforward, as it varies with the ions concentration decay in original brine with the increasing S_{NaCl}. In the NOCe, the Pe changes from the order of 10^2 (advective regime) during flowing episodes (i.e., V > 0), to null during interludes (i.e., V = 0), and the system is completely controlled by the diffusion (i.e., Da tends to infinity). Since this change in Pe is expected to enhance the homogenization of salt precipitation, it explains the S_{CO2} and S_{NaCl} backwards transition from $E1_{CO2}$ to E2 during Test-1 (Fig. 8a).

Overall, upon detection of CO_2-induced salt precipitation in a reservoir formation through seismic and electromagnetic geophysical surveys, reducing or stopping the CO_2 injection is advisable for high porosity and permeability reservoirs and low brine salinity (e.g., Sleipner CCS field[35]). However, stopping or reducing the CO_2 injection (i.e., minimum Pe; maximum Da), might have undesirable effects for reservoirs with lower porosity and permeability and higher brine salinity[8,56]. In these latter reservoirs, the higher capillarity of the rock could lead to self-enhancing salt growth phenomena[6], rather than salt reabsorption and homogenization, which would extend the salt precipitation to large sub-surface regions. In turn, this would reduce the effectiveness of common clogging mitigation techniques, such as fresh water flooding, mainly focused on the surroundings of the injection well.
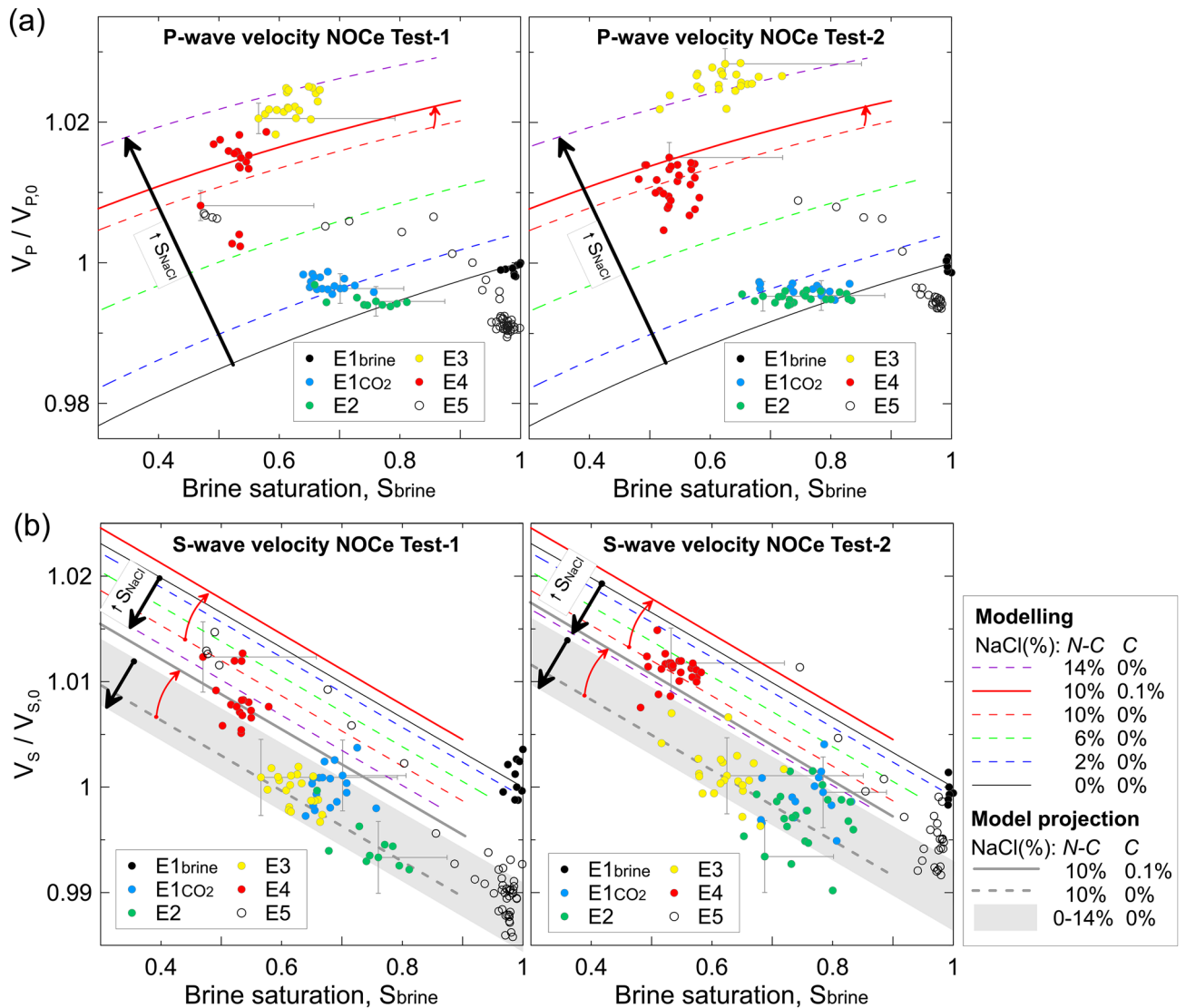
Figure 8. (a) Compressional and (b) shear ultrasonic wave velocity (V_P and V_S), normalized with respect to their original brine saturation (subscript 0) values for NOCe Test-1 and Test-2, versus brine saturation, S_{brine}, for the five episodes (E1–5) of both NOCe tests. The red arrow indicates the transition at S_{NaCl} 10% from non-cementing (N–C) to N–C with 0.1% of cementing salt (red model curves). To facilitate the analysis, we assume constant brine salinity of 25×10^4 ppm (i.e., minimum S_{brine} possible; see Fig. 7), and add one cross error bar per episode to account (horizontally) for the effect of ions depletion during salt precipitation and (vertically) the uncertainty around the ultrasonic velocity determinations.

Furthermore, salt would be prone to fill (micro-) pores and start cementing the rock, thus modifying rock mechanical properties. During the GCS post-injection stage, natural aquifer recharge might lead to re-dissolution of salt crystals, this time with permanent changes in rock mechanical properties, as suggested by the hysteresis shown by the axial strain (only ~ 5% recovery) during the NOCe, together with the V_P and V_S drop and the increase of the original porosity and permeability, during NOCe Test-1 and Test-2.

Conclusions

During a set of CO_2 flow-through experiments using a synthetic sandstone of well-known petrophysical properties, we have found evidence of CO_2-induced salt precipitation from X-ray micro-CT imaging and of detectable geophysical signatures (elastic waves and electrical resistivity) associated to this phenomenon. Our results show for the first time how elastic wave velocities, when combined with electrical resistivity measurements, can be used to detect early stage salt precipitation during CO_2 injection into reservoir sandstones. Based on our experimental results, we conclude:

1. The precipitation of salt induced by CO_2 injection into brine saturated sandstones significantly affects measurable geophysical properties of the original rock formation, i.e., compressional and shear wave velocity, and electrical resistivity. During early stage injection, salt precipitates away from grain contacts (non-cementing),

then starts to cement the rock grains after a certain threshold salt saturation is achieved (10% in our experiment).

2. The precipitation of salt triggers detectable changes in compressional wave velocity (up to 3%) that can be differentiated from pore fluid substitution effects with the aid of electrical resistivity, based on the latter's sensitivity to electrically insulating gas phases like CO_2. While compressional wave velocity is sensitive to both non-cementing and cementing salt precipitation, shear waves velocity is predominantly sensitive to the fraction of cementing salt.

3. During CO_2-induced salt precipitation, pore fluid salinity changes have to be considered to successfully estimate the evolution of CO_2, brine and salt saturations from electrical resistivity.

4. CO_2-induced salt precipitation may lead to dilation of the rock frame, even in high porosity and permeability sandstones that are barely reactive to CO_2. Hence, early detection of salt precipitation is crucial to preserve reservoir injectivity properties and mechanical integrity.

Materials and methods

Rock samples and pore fluid.
We created a homogeneous synthetic sandstone of high (effective) porosity ($\phi = 0.29$; He-pycnometry), and high absolute permeability $k_{abs} \sim 1660$ mD (N_2-permeameter), to avoid salt-induced clogging during CO_2 injection. Following the manufacturing procedure described in Falcon-Suarez, et al.[57], we used sorted, coarse grained (diameter > 500 μm) sand and low cement-to-grain ratio to ensure high porosity and permeability (with a final dry density $\rho_d \sim 1826$ kg m^{-3}) and to avoid clay conductivity and clogging effects. The composition of the sample was ~ 97% quartz, ~ 3% albite (X-ray diffraction, XRD, analysis with a Philips X'Pert pro XRD-Cu X-ray tube), which ensures the applicability of the original Archie's laws without applying corrections related to the presence of clay minerals in the rock. From the original sample, we extracted two core plugs of (sample A) 2 cm length, 1.2 cm diameter, and (sample B) 2 cm length, 5 cm diameter, for the CSMe test and for the NOCe tests, respectively.

We used a 25% NaCl synthetic brine solution prepared with deionized water in both tests, keeping NaCl concentration slightly below the saturation point to promote rapid crystallization during CO_2-induced evaporation. To ensure the saturation condition, the samples were first oven-dried, then saturated with the experimental brine via imbibition under vacuum conditions, and finally flushed at 5 MPa with the experimental brine solution to enhance the dissolution of remaining air in the system. At the pore pressure used in this test, the salinity of the brine has neglectable effect on the mutual solubility of CO_2 and brine.

CSMe setup and test configuration.
The brine saturated sample A contained in an in-house developed Aluminium pressure vessel was pressure equilibrated for one night at the target P_c (25 MPa) and P_p (5 MPa) conditions, and left for one night for stress–strain equilibrium. Then, the test started with a brine flow episode at 0.2 cm^3 min^{-1}, up to completing 17 PV of brine flow-through. Immediately after, the first XCT-scanning was carried out lasting ~ 24 h. Next, CO_2 was injected in the sample at variable flow rate (0.1—0.2 cm^3 min^{-1}) continuously during 24 h (Peclet's number Pe ~ 60), reaching ~ 200 PV of collected pore fluid volume downstream. Immediately after, the second XCT-scanning was conducted.

The pressure vessel setup consisted of an aluminium tube sealed with commercial high-pressure fittings, and three flow-through lines for confining, and inlet and outlet pore pressure. The sample A was jacketed and plugged with in-house manufactured endcaps, allowing pore fluid flow-through while isolating the sample from the confining hydraulic oil. Pressure vessel connecting lines were flexible to ensure free twisting of the vessel within the XCT instrument during XCT image acquisition. We performed the measurements using a Xradia Micro XCT-400. Tomographic images were collected in increments of 0.1 degrees of rotation with a background reference image generated from 10 averaged individual scans preceding installation of the pressure vessel. The reference image was subtracted from the measurement images to give adjusted values for the sample and vessel without background effects. Optimal tomography angles were calculated using specialist software XM-Controller 8.1.7546 (XRadia Inc.; https://www.zeiss.com/microscopy/int/products/x-ray-microscopy), and measurements were obtained with 0.5 × and 4 × lens yielding resolutions of approximately 25 and 3 microns, respectively. For this study, we only used the latter (high resolution image set). Tomographic images were generated following beam hardening and centre shift corrections to ensure optimal image quality in the reconstructed images, using Avizo software version 9.5.0 (https://www.fei.com/software/avizo-user-guide). The XCT-images were segmented using a 3D weka semi-automated segmentation[58] to characterize the four phases of interest: CO_2, brine, quartz and the rest, which included ore minerals and salt (Fig. 2). First, we selected a sub-sample (~ 1.5 mm^3) and obtained the four phases; second, we extrapolated the results to the whole sample, following the procedure described in Callow, et al.[59].

After the test, the sample was left to dry under atmospheric conditions. Then, thin sections were obtained from both the original and the tested samples, to assess the total salt content in the porous medium. The images were analysed using Fiji-ImageJ software version 2.0.0-rc-68/1.52 g (https://fiji.sc) to measure the total salt in the sample. The blue-resin method used to make the thin sections allowed the segmentation of the obtained in plane-polarized light images into four domains: pores (blue), grains (light grey), cement (brownish), and salt (black regions: isotropic salt crystals and ore minerals). The processing consisted of a threshold filtering to define the pores (ϕ) and salt (S) fractional areas, and then transform it to grey scale to calculate the salt saturation as $S_{NaCl} = S / (\phi + S)$.

NOCe setup and test configuration.
The rig is configured around a triaxial cell core holder under accurate control (ISCO pumps) of confining and pore pressure[31]. The rubber sleeve inside the vessel has 16 stainless steel electrodes connected to an electrical resistivity tomography data acquisition system[31,35]. Using a tetra-polar

electrode configuration, each run collects 208 individual (tetra-polar) measurements, which are then inverted using a variation of the software EIDORS (version 3.1) MATLAB toolkit (https://eidors3d.sf.net). Axially, two (confining) platens house ultrasonic pulse-echo sensors, isolated from the sample and the rest of the rig by two polyether ether ketone (PEEK) buffer rods of well-defined acoustic impedance and low energy loss. This configuration provides a reliable delay path within the frequency range 400–1000 kHz, which enables the identification of top/base sample reflections for calculating ultrasonic P- and S-wave velocities and attenuations using the pulse-echo technique[18,19], with ± 0.1% velocity precision and ± 0.3% accuracy (95% confidence), while up to ± 5% for the attenuation. The signals are displayed on a digital oscilloscope LeCroy Wavesurfer 4000HD (https://teledynelecroy.com/) and stored on the computer for spectral analysis assembly using MATLAB R2017a (https://www.mathworks.com). For this test, we processed the ultrasonic data from Fourier analysis of broad band signals to compare the ultrasonic properties of our three samples at a single frequency of 550 kHz.

The sample B was equipped with 350 Ohms electrical strain gauges, epoxy-glued on the lateral side of the sample, to record axial (ε_a) strains during the tests in continuous (every two seconds), with an accuracy of $\pm 10^{-6}$ m m^{-1} (i.e., < 1.5% error for the deformation range in our experiment; Fig. 5). The strain gauges limited the ERT interpretation to the vertical plane (i.e., 2D) elongated 90° with respect to the gauges position. Along with the strains, the pore pressure was also monitored with two additional pressure (piezoresistivity) sensors located directly up- and downstream of the sample. The injection of both the brine and CO$_2$ were carried out under controlled pore pressure downstream (5.5 MPa) and outlet flow. To avoid early compaction effects, the sample was initially placed into the triaxial vessel at the test conditions during four days, and then subjected to minimum brine flow-through (0.01 cm^3 min^{-1}). Injected confining fluid and the strains indicated mechanical stabilization occurred after two days. After the first test, the confining and pore pressure were dropped by keeping constant the differential pressure ($P_{diff} = P_c - P_p =$ constant, to minimize stress-induced damages), down to atmospheric P_p conditions. Then, first, the sample was newly saturated via vacuum imbibition under confining inside the vessel for ~ 3 h; next, under continuous brine flow, both P_c and P_p were again increased at constant P_{diff}, first up to $P_p = 10$ MPa (i.e., $P_c = 30$ MPa) during 1 h flow to enhance dissolution of any remaining CO$_2$ bubble, and finally to the original test conditions ($P_c = 25$ MPa and $P_p = 5$ MPa). Once at the test conditions, the CO$_2$ flow-through test was repeated, replicating the episodes of the first one. After the NOCe Test-2, the sample was batched in DIW for a week, and then dried to measure the final (subscript f) porosity ($\phi_f = 0.306$; He-pycnometry) and permeability ($k_{abs,f}$ ~ 1771 mD; N$_2$-permeameter).

Elastic wave modelling: rock with salt in the pores.   Our modelling of elastic wave parameters follows Ecker, et al.[51] approach that considers two idealized models for solid phase precipitation in the pores (gas hydrate in their case and salt in this work). We combine the stiff uncemented and cemented sand models[46,47] using MATLAB (R2017a) to calculate the frame properties of the dry rock, and applied Biot-Stoll[48-50] to calculate P and S-wave velocity and attenuation over the whole brine saturation range at a frequency of 550 kHz. Fluid density, viscosity and compressibility at the experimental pressure, temperature and salinity conditions were calculated using the High Pressure International EOS for brine[60] and data from the National Institute of Standards and Technology (https://webbook.nist.gov/chemistry/fluid/) for CO$_2$.

Data availability
Data presented in this study will be publically available: (1) the XCT data (CSMe tests) at the OSF (https://osf.io/) and the Colorado School of Mines website (https://crusher.mines.edu/publications/); and (2) the geophysical data (NOCe tests) at the UK National Geoscience Data Centre (NGDC) repository (https://doi.org/10.5285/6c9d05aa-f1f2-49a9-868e-3d2d5947ad54).

References
1. Michael, K. *et al.* Geological storage of CO$_2$ in saline aquifers: A review of the experience from existing storage operations. *Int. J. Greenh. Gas. Con.* **4**, 659–667. https://doi.org/10.1016/j.ijggc.2009.12.011 (2010).
2. Benson, S. M. & Cole, D. R. CO$_2$ sequestration in deep sedimentary formations. *Elements.* **4**, 325–331. https://doi.org/10.2113/gselements.4.5.325 (2008).
3. Rutqvist, J. The geomechanics of CO$_2$ storage in deep sedimentary formations. *Geotech. Geol. Eng.* **30**, 525–551. https://doi.org/10.1007/s10706-011-9491-0 (2012).
4. Chadwick, R. A., Williams, G. A. & Falcon-Suarez, I. Forensic mapping of seismic velocity heterogeneity in a CO$_2$ layer at the Sleipner CO$_2$ storage operation, North Sea, using time-lapse seismics. *Int. J. Greenh. Gas. Con.* **90**, 102793. https://doi.org/10.1016/j.ijggc.2019.102793 (2019).
5. Zhu, T., Ajo-Franklin, J., Daley, T. M. & Marone, C. Dynamics of geologic CO$_2$ storage and plume motion revealed by seismic coda waves. *Proc. Acad. Nat. Sci.* **116**, 2464–2469. https://doi.org/10.1073/pnas.1810903116 (2019).
6. Miri, R., van Noort, R., Aagaard, P. & Hellevang, H. New insights on the physics of salt precipitation during injection of CO$_2$ into saline aquifers. *Int. J. Greenh. Gas. Con.* **43**, 10–21. https://doi.org/10.1016/j.ijggc.2015.10.004 (2015).
7. Miri, R. & Hellevang, H. Salt precipitation during CO$_2$ storage—A review. *Int. J. Greenh. Gas. Con.* **51**, 136–147. https://doi.org/10.1016/j.ijggc.2016.05.015 (2016).
8. Grude, S., Landrø, M. & Dvorkin, J. Pressure effects caused by CO$_2$ injection in the Tubåen Fm., the Snøhvit field. *Int. J. Greenh. Gas. Con.* **27**, 178–187, https://doi.org/10.1016/j.ijggc.2014.05.013 (2014).
9. Bacci, G., Durucan, S. & Korre, A. Experimental and numerical study of the effects of halite scaling on injectivity and seal performance during CO$_2$ injection in saline aquifers. *Energy. Proc.* **37**, 3275–3282. https://doi.org/10.1016/j.egypro.2013.06.215 (2013).
10. Ott, H., Andrew, M., Snippe, J. & Blunt, M. J. Microscale solute transport and precipitation in complex rock during drying. *Geophys. Res. Lett.* **41**, 8369–8376. https://doi.org/10.1002/2014gl062266 (2014).

11. André, L., Peysson, Y. & Azaroual, M. Well injectivity during CO_2 storage operations in deep saline aquifers—Part 2: Numerical simulations of drying, salt deposit mechanisms and role of capillary forces. *Int. J. Greenh. Gas. Con.* **22**, 301–312. https://doi.org/10.1016/j.ijggc.2013.10.030 (2014).

12. Roels, S. M., Ott, H. & Zitha, P. L. J. μ-CT analysis and numerical simulation of drying effects of CO_2 injection into brine-saturated porous media. *Int. J. Greenh. Gas. Con.* **27**, 146–154. https://doi.org/10.1016/j.ijggc.2014.05.010 (2014).

13. Liu, H.-H., Zhang, G., Yi, Z. & Wang, Y. A permeability-change relationship in the dryout zone for CO_2 injection into saline aquifers. *Int. J. Greenh. Gas. Con.* **15**, 42–47. https://doi.org/10.1016/j.ijggc.2013.01.034 (2013).

14. Zeidouni, M., Pooladi-Darvish, M. & Keith, D. Analytical solution to evaluate salt precipitation during CO_2 injection in saline aquifers. *Int. J. Greenh. Gas. Con.* **3**, 600–611. https://doi.org/10.1016/j.ijggc.2009.04.004 (2009).

15. Bacci, G., Korre, A. & Durucan, S. Experimental investigation into salt precipitation during CO_2 injection in saline aquifers. *Energy. Proc.* **4**, 4450–4456. https://doi.org/10.1016/j.egypro.2011.02.399 (2011).

16. Kleinitz, W., Dietzsch, G. & Köhler, M. Halite scale formation in gas-producing wells. *Chem. Eng. Res. Des.* **81**, 352–358. https://doi.org/10.1205/02638760360596900 (2003).

17. Pruess, K. & Müller, N. Formation dry-out from CO_2 injection into saline aquifers: 1. Effects of solids precipitation and their mitigation. *Water Resour. Res.* **45**, https://doi.org/10.1029/2008WR007101 (2009).

18. Kim, K.-Y., Han, W. S., Oh, J., Kim, T. & Kim, J.-C. Characteristics of salt-precipitation and the associated pressure build-up during CO_2 storage in saline aquifers. *Transport. Porous. Med.* **92**, 397–418. https://doi.org/10.1007/s11242-011-9909-4 (2012).

19. Guyant, E., Han, W. S., Kim, K.-Y., Park, M.-H. & Kim, B.-Y. Salt precipitation and CO_2/brine flow distribution under different injection well completions. *Int. J. Greenh. Gas. Con.* **37**, 299–310. https://doi.org/10.1016/j.ijggc.2015.03.020 (2015).

20. Kim, M., Sell, A. & Sinton, D. Aquifer-on-a-chip: Understanding pore-scale salt precipitation dynamics during CO_2 sequestration. *Lab. Chip.* **13**, 2508–2518. https://doi.org/10.1039/C3LC00031A (2013).

21. Sokama-Neuyam, Y., Ursin, J. & Boakye, P. Experimental investigation of the mechanisms of salt precipitation during CO_2 injection in sandstone. *J. Carbon. Res.* **5**, 4. https://doi.org/10.3390/c5010004 (2019).

22. Ott, H., Roels, S. M. & de Kloe, K. Salt precipitation due to supercritical gas injection: I. Capillary-driven flow in unimodal sandstone. *Int. J. Greenh. Gas. Con.* **43**, 247–255, https://doi.org/10.1016/j.ijggc.2015.01.005 (2015).

23. Peysson, Y., André, L. & Azaroual, M. Well injectivity during CO_2 storage operations in deep saline aquifers—Part 1: Experimental investigation of drying effects, salt precipitation and capillary forces. *Int. J. Greenh. Gas. Con.* **22**, 291–300. https://doi.org/10.1016/j.ijggc.2013.10.031 (2014).

24. Giorgis, T., Carpita, M. & Battistelli, A. 2D modeling of salt precipitation during the injection of dry CO_2 in a depleted gas reservoir. *Energy. Convers. Manag.* **48**, 1816–1826. https://doi.org/10.1016/j.enconman.2007.01.012 (2007).

25. Mahadevan, J., Sharma, M. M. & Yortsos, Y. C. Water removal from porous media by gas injection: Experiments and simulation. *Transport. Porous. Med.* **66**, 287–309. https://doi.org/10.1007/s11242-006-0030-z (2007).

26. Nooraiepour, M., Fazeli, H., Miri, R. & Hellevang, H. Effect of CO_2 phase states and flow rate on salt precipitation in shale caprocks—A microfluidic study. *Environ. Sci. Technol.* **52**, 6050–6060. https://doi.org/10.1021/acs.est.8b00251 (2018).

27. Muller, N., Qi, R., Mackie, E., Pruess, K. & Blunt, M. J. CO_2 injection impairment due to halite precipitation. *Energy. Proc.* **1**, 3507–3514. https://doi.org/10.1016/j.egypro.2009.02.143 (2009).

28. Saxena, N., Mavko, G., Hofmann, R. & Srisutthiyakorn, N. Estimating permeability from thin sections without reconstruction: Digital rock study of 3D properties from 2D images. *Comput. Geosci.* **102**, 79–99. https://doi.org/10.1016/j.cageo.2017.02.014 (2017).

29. Zhang, Y. *et al.* The pathway-flow relative permeability of CO2: Measurement by lowered pressure drops. *Water Resour. Res.* **53**, 8626–8638. https://doi.org/10.1002/2017wr020580 (2017).

30. Krevor, S. *et al.* Capillary trapping for geologic carbon dioxide storage—From pore scale physics to field scale implications. *Int. J. Greenh. Gas. Con.* **40**, 221–237. https://doi.org/10.1016/j.ijggc.2015.04.006 (2015).

31. Falcon-Suarez, I. *et al.* Experimental assessment of pore fluid distribution and geomechanical changes in saline sandstone reservoirs during and after CO_2 injection. *Int. J. Greenh. Gas. Con.* **63**, 356–369. https://doi.org/10.1016/j.ijggc.2017.06.019 (2017).

32. Noiriel, C., Renard, F., Doan, M.-L. & Gratier, J.-P. Intense fracturing and fracture sealing induced by mineral growth in porous rocks. *Chem. Geol.* **269**, 197–209. https://doi.org/10.1016/j.chemgeo.2009.09.018 (2010).

33. Desarnaud, J., Bonn, D. & Shahidzadeh, N. The pressure induced by salt crystallization in confinement. *Sci. Rep.* **6**, 30856. https://doi.org/10.1038/srep30856 (2016).

34. Alemu, B. L., Aker, E., Soldal, M., Johnsen, Ø & Aagaard, P. Effect of sub-core scale heterogeneities on acoustic and electrical properties of a reservoir rock: A CO_2 flooding experiment of brine saturated sandstone in a computed tomography scanner. *Geophys. Prospect.* **61**, 235–250. https://doi.org/10.1111/j.1365-2478.2012.01061.x (2013).

35. Falcon-Suarez, I. *et al.* CO_2-brine flow-through on an Utsira Sand core sample: Experimental and modelling. Implications for the Sleipner storage field. *Int. J. Greenh. Gas. Con.* **68**, 236–246, https://doi.org/10.1016/j.ijggc.2017.11.019 (2018).

36. Kim, J., Nam, M. J. & Matsuoka, T. Estimation of CO_2 saturation during both CO_2 drainage and imbibition processes based on both seismic velocity and electrical resistivity measurements. *Geophys. J. Int.* **195**, 292–300. https://doi.org/10.1093/gji/ggt232 (2013).

37. Lei, X. & Xue, Z. Ultrasonic velocity and attenuation during CO_2 injection into water-saturated porous sandstone: Measurements using difference seismic tomography. *Phys. Earth. Planet. In.* **176**, 224–234. https://doi.org/10.1016/j.pepi.2009.06.001 (2009).

38. Vanorio, T., Nur, A. & Ebert, Y. Rock physics analysis and time-lapse rock imaging of geochemical effects due to the injection of CO_2 into reservoir rocks. *Geophysics* **76**, 23–33. https://doi.org/10.1190/geo2010-0390.1 (2011).

39. Nakatsuka, Y., Xue, Z., Garcia, H. & Matsuoka, T. Experimental study on CO_2 monitoring and quantification of stored CO_2 in saline formations using resistivity measurements. *Int. J. Greenh. Gas. Con.* **4**, 209–216. https://doi.org/10.1016/j.ijggc.2010.01.001 (2010).

40. Archie, G. E. The electrical resistivity log as an aid in determining some reservoir characteristics. *Soc. Pet. Eng. J.* https://doi.org/10.2118/942054-G (1942).

41. Canal, J. *et al.* Injection of CO_2-saturated water through a siliceous sandstone plug from the Hontomin test site (Spain): Experiment and modeling. *Environ. Sci. Technol.* **47**, 159–167. https://doi.org/10.1021/es3012222 (2013).

42. Duan, Z., Sun, R., Zhu, C. & Chou, I. M. An improved model for the calculation of CO_2 solubility in aqueous solutions containing Na^+, K^+, Ca^{2+}, Mg^{2+}, Cl^-, and SO_4^{2-}. *Mar. Chem.* **98**, 131–139. https://doi.org/10.1016/j.marchem.2005.09.001 (2006).

43. Crain, E. in *Crain's Petrophysical Handbook* (2002).

44. Gassmann, F. Elastic waves through a packing of spheres. *Geophysics* **16**, 673–685. https://doi.org/10.1190/1.1437718 (1951).

45. Mavko, G. & Mukerji, T. Bounds on low-frequency seismic velocities in partially saturated rocks. *Geophysics* **63**, 918–924. https://doi.org/10.1190/1.1444402 (1998).

46. Mavko, G., Mukerji, T. & Dvorkin, J. *Rock Physics Handbook—Tools for Seismic Analysis in Porous Media*. (Cambridge University Press, 2009).

47. Dvorkin, J. & Nur, A. Elasticity of high-porosity sandstones; theory for two North Sea data sets. *Geophysics* **61**, 1363–1370. https://doi.org/10.1190/1.1444059 (1996).

48. Biot, M. A. Theory of propagation of elastic waves in a fluid-saturated porous solid. I. Low-frequency range. *J. Acoust. Soc. Am.* **28**, 168–178, https://doi.org/10.1121/1.1908239 (1956).

49. Biot, M. A. Theory of propagation of elastic waves in a fluid-saturated porous solid. II. Higher frequency range. *J. Acoust. Soc. Am.* **28**, 179–191, https://doi.org/10.1121/1.1908241 (1956).

50. Stoll, R. D. & Bryan, G. M. Wave attenuation in saturated sediments. *J. Acoust. Soc. Am.* **47**, 1440–1447. https://doi.org/10.1121/1.1912054 (1970).
51. Ecker, C., Dvorkin, J. & Nur, A. Sediments with gas hydrates: Internal structure from seismic AVO. *Geophysics* **63**, 1659–1669. https://doi.org/10.1190/1.1444462 (1998).
52. Marín-Moreno, H., Sahoo, S. K. & Best, A. I. Theoretical modeling insights into elastic wave attenuation mechanisms in marine sediments with pore-filling methane hydrate. *J. Geophys. Res. Solid. Earth.* **122**, 1835–1847. https://doi.org/10.1002/2016jb013577 (2017).
53. Luquot, L. & Gouze, P. Experimental determination of porosity and permeability changes induced by injection of CO_2 into carbonate rocks. *Chem. Geol.* **265**, 148–159. https://doi.org/10.1016/j.chemgeo.2009.03.028 (2009).
54. Huinink, H. P., Pel, L. & Michels, M. A. J. How ions distribute in a drying porous medium: A simple model. *Phys. Fluids.* **14**, 1389–1395. https://doi.org/10.1063/1.1451081 (2002).
55. Naillon, A., Joseph, P. & Prat, M. Sodium chloride precipitation reaction coefficient from crystallization experiment in a microfluidic device. *J. Cryst. Growth.* **463**, 201–210. https://doi.org/10.1016/j.jcrysgro.2017.01.058 (2017).
56. Baumann, G., Henninges, J. & De Lucia, M. Monitoring of saturation changes and salt precipitation during CO_2 injection using pulsed neutron-gamma logging at the Ketzin pilot site. *Int. J. Greenh. Gas. Con.* **28**, 134–146. https://doi.org/10.1016/j.ijggc.2014.06.023 (2014).
57. Falcon-Suarez, I. H. *et al.* Comparison of stress-dependent geophysical, hydraulic and mechanical properties of synthetic and natural sandstones for reservoir characterization and monitoring studies. *Geophys. Prospect.* **67**, 784–803. https://doi.org/10.1111/1365-2478.12699 (2019).
58. Arganda-Carreras, I. *et al.* Trainable Weka segmentation: A machine learning tool for microscopy pixel classification. *Bioinformatics* **33**, 2424–2426. https://doi.org/10.1093/bioinformatics/btx180 (2017).
59. Callow, B., Falcon-Suarez, I., Ahmed, S. & Matter, J. M. Assessing the carbon sequestration potential of basalt using X-ray micro-CT and rock mechanics. *Int. J. Greenh. Gas. Con.* **70**, 146–156. https://doi.org/10.1016/j.ijggc.2017.12.008 (2018).
60. Millero, F. J., Chen, C.-T., Bradshaw, A. & Schleicher, K. A new high pressure equation of state for seawater. *Deep-Sea. Res. Pt.* **27**, 255–264. https://doi.org/10.1016/0198-0149(80)90016-3 (1980).

Acknowledgements

Author contributions

I.H.F.S contribution roles include conceptualization, data curation, formal analysis, funding acquisition, investigation, methodology, project administration resources, validation, visualization and writing—original draft; K.L. contribution roles include conceptualization, methodology, supervision, visualization and writing—review & editing; H.M.M. contribution roles include software, validation and writing—review & editing; B.C. contribution roles include data curation, formal analysis and writing—review & editing; M.P. contribution roles include funding acquisition, resources, supervision and writing—review & editing; A.B. contribution roles include funding acquisition, resources, supervision and writing—review & editing.

Competing interests

The authors declare no competing interests.

Additional information

Supplementary information is available for this paper at https://doi.org/10.1038/s41598-020-73091-3.

Correspondence and requests for materials should be addressed to I.H.F.-S.

Reprints and permissions information is available at www.nature.com/reprints.

Publisher's note Springer Nature remains neutral with regard to jurisdictional claims in published maps and institutional affiliations.